Journal of Alloys and Compounds 822 (2020) 153514

Contents lists available at ScienceDirect

Journal of Alloys and Compounds

journal homepage: http://www.elsevier.com/locate/jalcom

Synthesis, structure and optical properties of (Mn/Cu) co-doped ZnO nanoparticles

S.D. Senol [a], E. Ozugurlu [b], L. Arda [c], *

[a] Bolu Abant Izzet Baysal University, Faculty of Arts & Science, Department of Chemistry, 14280, Bolu, Turkey
[b] Istanbul Technical University, Department of Mathematics, 34469, Maslak, Istanbul, Turkey
[c] Bahcesehir University, Faculty of Engineering and Natural Sciences, Department of Mechatronic Engineering, 34349, Besiktas, Istanbul, Turkey

ARTICLE INFO

Article history:
Received 8 August 2019
Received in revised form
21 December 2019
Accepted 23 December 2019
Available online 25 December 2019

Keywords:
Zinc oxide
Nanoparticles
Photoluminescence
Energy gap
Refractive index

ABSTRACT

Mn/Cu co-doped ZnO ($Zn_{0.99-x}Mn_xCu_{0.01}O$) nanoparticles were synthesized by the solid state reaction method to investigate the relationship between the band gap and the refractive index. The stoichiometry was provided by increasing x values (x = 0.00, 0.01, 0.02, 0.03, 0.04, and 0.05). The X-ray diffraction (XRD) method was utilized for the structural analysis of all Mn/Cu co-doped ZnO nanoparticles. Hexagonal Wurtzite structure was established by making use of the c/a ratios of the ZnMnCuO nanoparticles. Photoluminescence (PL) properties were measured by employing the Agilent Cary Eclipse Fluorescence Spectrophotometer to discover the structural defects. The red emission with its wavelength within the range of 620–750 nm was observed. The red emission centered at 700 nm could be attributed to oxygen vacancy (V_o) which was strongly dependent on the Mn concentration. The Fourier Transform Infra-Red (FT-IR) spectra (4000 - 400 cm^{-1}) of the samples were recorded in the By PerkinElmer Spectrum Two FTIR-ATR spectrophotometer. Scanning Electron Microscope (SEM) technique was applied to determine the surface morphology, crystallite size, and the shapes of the nanoparticles. The elemental compositions of the nanoparticles were obtained by Electron Dispersive Spectroscopy (EDAX). The optical properties of the nanoparticles were obtained by using the Shimadzu 2600 Ultraviolet–Visible (UV-VIS) Spectrophotometer. The energy band gaps of the samples were calculated and the effects of dopant elements on optical properties were discussed. The refractive index was calculated by using the five different models. The maximum band gap occurred for $Zn_{0.97}Mn_{0.02}Cu_{0.01}O$ with a band gap energy of $E_g = 3.28$ eV.

1. Introduction

There has been a great interest in high refractive index *n* and wide band gap E_g because of their applications in optoelectronic and sensor industries. To increase the performance of optical interference filters and optical sensors (e.g. anti-reflection coatings), there is a need not only for the high refractive index but also for wide band gap materials.

Recently, Naccarato et al. [1] in 2019 published an article to relate the high refraction index and band gap, for which they evaluated more than 4000 semiconductors and investigated how the chemistry influenced this inverse relationship between refraction index and band gap and rationalized why certain classes of materials would perform better. The energy gap forms the threshold for absorption of photons in semiconductors. The refractive index in the semiconductor is a measure of its transparency to incident spectral radiation. A correlation between these two fundamental properties has a significant bearing on the band structure of semiconductors. Naccarato et al. [1] reviewed some of the refractive index calculation models proposed by, namely, Ravindra et al. [2], Moss [3], Hervé and Vandamme [4], Reddy and Anjayenulu [5], Kumar and Singh [6]. Especially, zinc oxide (ZnO) is emphasized as a favorable choice for functional components of devices and materials in photonic crystals [7,8], spintronics [9], gas sensors [10], light-emitting diodes [11,12], microelectronics, solar cells [13], lasers [14], varistors [15] and photoelectrochemical cells [16]. In addition, it is one of the crucial and emerging semiconductor materials with a direct band gap of ~3.37 eV and a large exciton binding energy of ~60 meV [17] at room temperature (RT). Moreover, since ZnO is a non-toxic, biocompatible, and biosafe material, it has been used as a drug carrier, a cosmetic, and a filling in medical applications.

---

* Corresponding author.
E-mail address: lutfi.arda@eng.bau.edu.tr (L. Arda).

https://doi.org/10.1016/j.jallcom.2019.153514
0925-8388/

To control the band gap, the electrical conductivity, and to increase the carrier concentration, it is important to determine with what element or elements ZnO must be doped. Lately, many researchers have concentrated on the doping of ZnO with transition metals (TMs) such as Mn, Ni, Fe, Cu, Co and Cr due to the potential applications in spintronics [18–22]. Among the various doping elements, Cu is nearly ideal for modifying the properties of ZnO because Cu atoms have a radius and electronic shell similar to those of Zn atoms; thus, the substitution of Zn by Cu does not induce a change in the lattice constant. Therefore, the effects of Cu doping on the magnetism, photoluminescence, band gap, and transmittance of ZnO films prepared by magnetron RF sputtering, magnetron DC sputtering, spray pyrolysis, pulsed laser deposition, and sol-gel processes have been heavily studied [23] and the references therein].

In 2011, Reddy et al. reported that when Cu^{2+} ions were located at substitution sites, the carrier concentration increased; as a result, the band-gap energy decreased. Cu-doped ZnO nanoparticles with 40 nm size were synthesized by the solution combustion method which showed a red shift and a narrowing of band gap [24]. According to Tao et al. [25], copper is a prominent luminescence activator, which can modify the luminescence of ZnO crystals by creating localized impurity levels. Kumar et al. [26] used Raman Spectroscopy to study the crystalline quality, structural disorder, and defects in the host lattice of the sol–gel derived $Zn_{1-x}Mn_xO$ ($0 \le x \le 0.06$) nanoparticles. Tiwari et al. [27] investigated (Ni, Cu) co-doped ZnO nanocrystals which were prepared by the wet chemical route. Their XRD measurements showed that though phase purity of the ZnO samples was retained by Ni doping at 2%, Cu doping beyond 3% created a separate CuO phase in the samples. Sharma and Jha [28] stated that Co/Mn co-doped ZnO nanocrystalline samples with tuned optical properties were promising candidates for applications in spintronic, optoelectronic devices (e.g. dye/quantum dot sensitized solar cells) and ceramics. Dubey et al. [29] investigated $Zn_{1-y-x}Mn_yLi_xO$ ($y = 0$, 0.02 and $x = 0$, 0.01, 0.02, 0.03, 0.04, 0.06) nanoparticles by the sol-gel method and concluded that these synthesized materials with visible light emission and dye degradation activity could be used effectively in future optoelectronic devices and in water purification for cleaning of dyes. Tamura and Ozaki [30] studied the electronic density of states and the magnetic properties of a series of 3d transition-metal (Mn, Fe, Co)-doped ZnO by tunneling spectroscopy and SQUID, respectively. The magnetization curve (M versus H) obtained by SQUID showed ferromagnetic hysteresis at room temperature for the Fe-doped sample superimposed on a linear characteristic, whereas for Mn- and Co-doped samples, the M versus H curve showed only the linear characteristic without hysteresis. There have been different approaches to the defect chemistry of Mn-doped ZnO. Cao et al. [31] assumed that doping of ZnO with manganese dominantly formed Mn^{2+} with a small amount of Mn^{4+}. According to their model, when Mn^{4+} ions replaced Zn^{2+} ions, they acted as donor atoms generating two free electrons while Mn^{2+} ions only generated oxygen vacancies.

It is known that the transition metals such as Cu and Mn are attractive dopants for ZnO, the reasons for which can be listed as follows: (i) they are isomorphic to Zn; (ii) they possess variable oxidation states, which are important for catalytic and photocatalytic applications; (iii) both of them have different acceptor properties into a ZnO matrix (except Mn in its lower oxidation state and Mn^{4+} when substituting Zn^{2+} ions), thus affecting the electronic surface band structure of ZnO, and consequently its applications.

In this study, $Zn_{0.99-x}Mn_xCu_{0.01}O$ nanoparticles were synthesized using the solid state reaction method by varying the dopant ratio from $x = 0.01$ to 0.05 in increments of 0.01. The structural and optoelectronic properties such as refractive index, band gap and reflectance spectra of the samples were calculated by using five different models, namely, those of Ravindra et al. [2], Moss [3], Hervé and Vandamme [4], Reddy and Anjayenulu [5], Kumar and Singh [6]. Moreover, we used the photoluminescence analysis to find the key factors affecting optical and structural performances. Since very few research articles report the strong co-emission of Ultraviolet (UV), blue, green and red light, by encompassing key results on how much the Mn concentration affects the red emission region centered at 700 nm, some light is shed on that issue.

2. Experimental procedures

2.1. Preparation of $Zn_{0.99-x}Mn_xCu_{0.01}O$ ($x = 0.00$, 0.01, 0.02, 0.03, 0.04, 0.05) nanoparticles

$Zn_{0.99}Cu_{0.01}O$ and $Zn_{0.99-x}Mn_xCu_{0.01}O$ ($x = 0.01$, 0.02, 0.03, 0.04, 0.05) nanoparticles with Cu doping concentration of 1 wt % and with Mn doping concentrations of 1, 2, 3, 4 and 5 wt % were prepared by solid state reaction method. Zinc acetate dehydrate ($Zn(CH_3CO_2)_2.2H_2O$ (Sigma Aldrich > 99% purity), copper(II)acetate ($Cu(CO_2CH_3)_2$ (Sigma Aldrich > 98% purity), manganese(II) acetate tetrahydrate ($Mn(CH_3COO)_2.4H_2O$) (Sigma Aldrich > 99% purity), were used as precursors. Firstly, 0.8691 g (99 wt %) zinc acetate dehydrate and 0.00798g (1 wt %) copper (II) acetate were mixed until finely powdered. Then, zinc acetate dehydrate (0.8603 g, 98 wt %), manganese (II) acetate tetrahydrate (0.01072 g, 1 wt %) and copper (II) acetate (0.00798 g, 1 wt %) were grounded together in an agate mortar until a homogeneous mixture was obtained. The other samples were prepared in the same manner. Afterwards, the mixtures were transferred into a porcelain crucible and put into a furnace for heating process. The prepared powders were heat treated at 600 °C for 2 h. The grey powders thus obtained were labeled $Zn_{0.99}Cu_{0.01}O$, $Zn_{0.98}Mn_{0.01}Cu_{0.01}O$, $Zn_{0.97}Mn_{0.02}Cu_{0.01}O$, $Zn_{0.96}Mn_{0.03}Cu_{0.01}O$, $Zn_{0.95}Mn_{0.04}Cu_{0.01}O$ and $Zn_{0.94}Mn_{0.05}Cu_{0.01}O$.

2.2. Characterization techniques

The phase characterizations of the powders thus prepared were carried out using Rigaku Multiflex diffractometer using CuK_α radiation ($\lambda = 1.5406$ Å), in the scan range of 2θ between 20^0 and 80^0 with a scan speed of 3°/min and with increments of 0.02. The surface morphologies of the obtained products were ascertained by scanning electron microscopy (SEM) and elemental analysis using X-ray energy distribution (EDAX) (FEI Quanta Feg250). The optical properties of the nanoparticles were established in the range of 200–900 nm with the help of Shimadzu 2600 UV-Spectrophotometer. The FT-IR spectra (4000 - 400 cm^{-1}) of the samples were recorded in the By PerkinElmer Spectrum Two FTIR-ATR spectrophotometer. Photoluminescence properties were assessed by using the Agilent Cary Eclipse Fluorescence Spectrophotometer.

3. Results and discussion

3.1. Structural characterization

XRD analysis was used to determine the structural behavior of all samples in the range of $20^\circ \le 2\theta \le 80^\circ$ degrees with indexed peak positions. As shown in Fig. 1 ZnO phase with wurtzite hexagonal structure (ICDD card No. 36–1451) of space group P63mc and the Mn_2O_3 [32] (ICDD card No. 76–0150) XRD patterns as the second phase were observed. Using XRD analysis of $Zn_{0.99}Cu_{0.01}O$ and $Zn_{0.99-x}Mn_xCu_{0.01}O$ ($x = 0.01$, 0.02, 0.03, 0.04, 0.05)

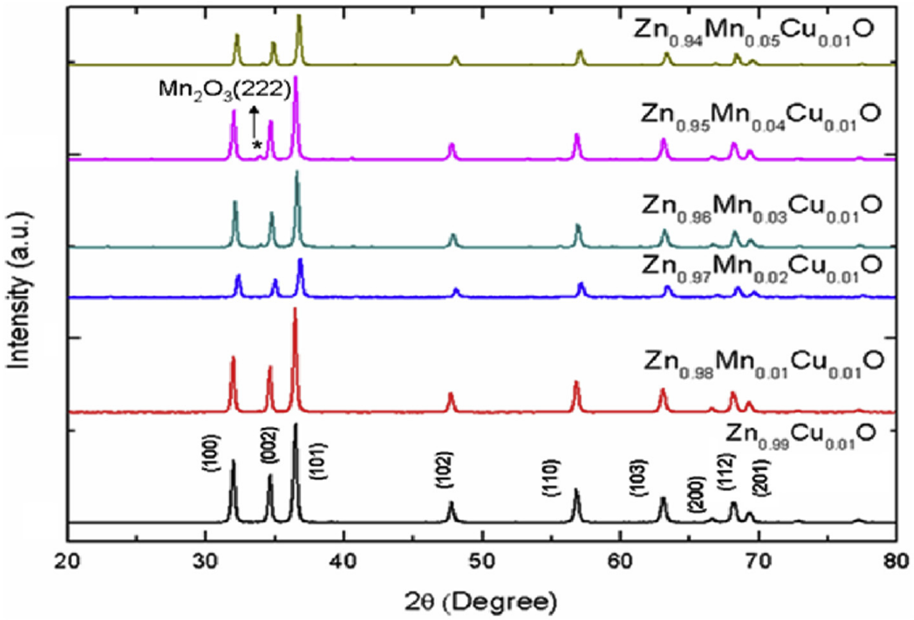

Fig. 1. XRD patterns of $Zn_{0.99-x}Mn_xCu_{0.01}O$ nanoparticles at different Mn concentrations.

nanoparticles, the concentration-dependent average crystallite sizes, lattice parameters, volume of the unit cell, microstrain (ε), stress (σ), dislocation density (δ) (the amount of defect in the sample), the locality of the atoms and their displacement (u), and bond length L were calculated and listed in Table 1 and shown in Figs. 2-4. The detailed calculations of ε, σ, δ, D, u, and L parameters may be found in Ref. [18].

As for Mn/Cu co-doped ZnO nanoparticles, the lattice parameter *c* calculated from the (002) peaks of the samples is in the range of 5.13–5.19 Å. There seems to be a fluctuation in c/a lattice parameter ratio. Such fluctuations are to be expected if Mn and Cu ions replace Zn ions in the lattice, as the Mn (0.66 Å) and Cu (0.73 Å) ions have smaller ionic radii than Zn ions (0.74 Å) [33].

The maximum microstrain ε occurred at $x = 0.02$. As can be seen in Table 2, the negative signs of σ values depict compressive stresses and these values exhibit a decrease until $x = 0.02$ dopant rate and beyond that, they fluctuate until a minimum value of −6.362 is reached. The fluctuations in the strain and stress values may reveal many physical defects and dislocations in the host lattice structure. Therefore, dislocation density (δ) describing the amount of defects in the sample were also studied. As shown in Table 2, the sizes (D) of the crystallite samples ~~are~~ fluctuated proportional to the increase of Mn in the stoichiometric samples. The maximum crystallite size (40.82 nm) occurred at $x = 0.03$. At $x = 0.03$, dislocation density (δ) displayed a minimum value of 6.01×10^{-4} due to the inverse proportion expression between δ and D values. The locality of the atoms and their displacements (u parameters) were calculated and revealed almost a constant behavior around 0.379 in $Zn_{0.99-x}Mn_xCu_{0.01}O$ samples. The Zn–O bond lengths (L parameters) presented a fluctuating behavior in the range of 1.948–1.963.

Table 1
Concentration dependent average crystallite sizes, lattice parameters, atomic packing. factor (c/a), crystal lattice distortion degree and volume of the unit cell in $Zn_{1-x}Mn_xCu_{0.01}O$ (x = 0.00, 0.01, 0.02, 0.03, 0.04, 0.05) nanoparticles.

Sample Name	D (nm)	a (Å)	c (Å)	c/a	R	Volume V(Å^3)
$Zn_{0.99}Cu_{0.01}O$	34.96	3.226	5.172	1.603	1.019	46.29
$Zn_{0.98}Mn_{0.01}Cu_{0.01}O$	39.94	3.227	5.176	1.604	1.018	46.35
$Zn_{0.97}Mn_{0.02}Cu_{0.01}O$	34.70	3.190	5.188	1.626	1.004	45.40
$Zn_{0.96}Mn_{0.03}Cu_{0.01}O$	40.82	3.214	5.154	1.604	1.018	45.79
$Zn_{0.95}Mn_{0.04}Cu_{0.01}O$	37.06	3.224	5.166	1.602	1.019	46.18
$Zn_{0.94}Mn_{0.05}Cu_{0.01}O$	37.92	3.199	5.132	1.604	1.018	45.17

ZnO bond length is calculated by the following Eq. (1) [18,34];

$$L = \sqrt{\left(\frac{a^2}{3}\right) + [0.5 - u]^2 c^2} \tag{1}$$

where a and c are lattice constants of ZnO and u is the wurtzite structure which can be the calculated by using Eq. (2);

$$u = \left(\frac{a^2}{3c^2}\right) + 0.25 \tag{2}$$

The lattice constants *a* for <100> and *c* for <002> planes are computed from Eq. (3) [18,35]:

$$\frac{1}{d_{\mathrm{hkl}}^2} = \frac{4}{3}\left(\frac{\mathrm{h}^2 + \mathrm{hk} + \mathrm{k}^2}{\mathrm{a}^2}\right) + \frac{\mathrm{l}^2}{\mathrm{c}^2} \tag{3}$$

The average crystallite size was assessed from the XRD peak width of ⟨101⟩ based on the Debye–Scherrer Eq. (4) [18,22],

$$D = \frac{K\,\lambda}{\beta_{\mathrm{hkl}} \cos(\theta)} \tag{4}$$

where β_{hkl} is the integral half width, K is a constant equal to 0.90, λ is the wavelength of the incident X-ray (λ = 0.1540 nm), D is the crystallite size, and θ is the Bragg angle.

The average crystallite size assessed for synthesized ZnO nanoparticles was 27.49 nm. The crystallite size is assumed to be that of a coherently diffracting domain and it is not necessarily same thing as the particle size. It can be seen that an ideal value for a single position parameter u of 3/8 = 0.375 (i.e. c/a = 1.63) is attainable for Mn concentration level of 2% and if the doping ratio is increased over and above that level, this increase causes the ideal value to degenerate. This degeneration might be a result of the

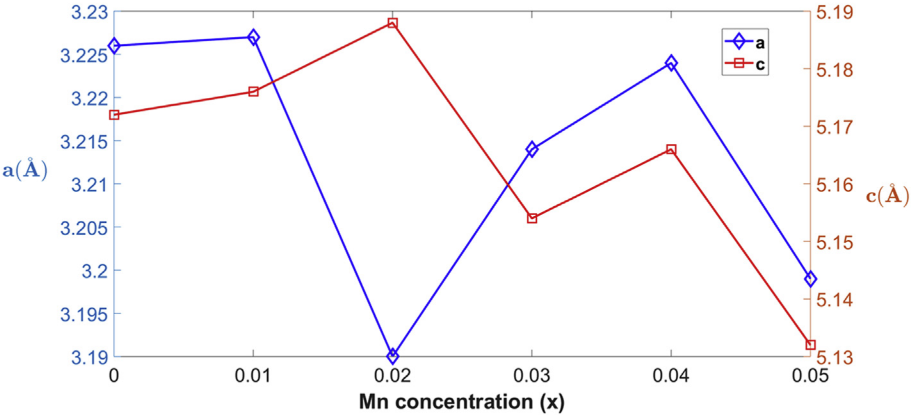

Fig. 2. Concentration-dependent lattice parameters (*a* and *c*) in $Zn_{0.99\text{-}x}Mn_xCu_{0.01}O$ structures.

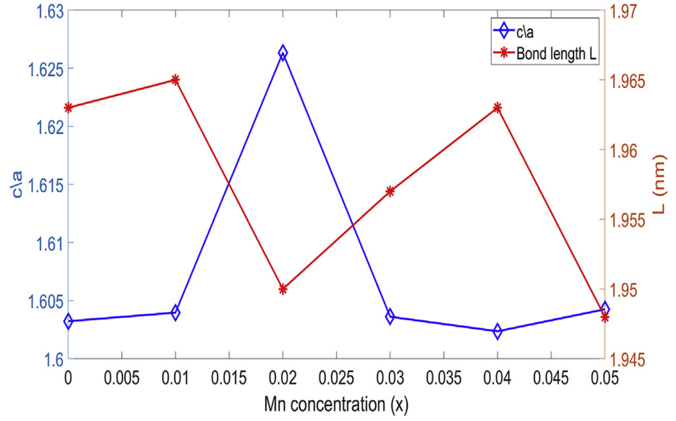

Fig. 3. Concentration-dependent lattice parameters (*c/a*) values and Zn—O bond lengths (*L*) variation in $Zn_{0.99\text{-}x}Mn_xCu_{0.01}O$ structures (x = 0.00, 0.01, 0.02, 0.03, 0.04, 0.05).

Table 2
The varying of concentration-dependent micro strain (Ɛ), stress (σ), dislocation density (δ) (the amount of defect in the sample), the locality of the atoms and their displacement (u), and bond length (L) in $Zn_{1-x}Mn_xCu_{0.01}O$ (x = 0.00, 0.01, 0.02, 0.03, 0.04, 0.05) nanoparticles.

Sample Name	Ɛ	$\sigma*10^9$ (N/m^2)	δ (nm^{-2})	u	L (Å)
$Zn_{0.99}Cu_{0.01}O$	0.072	−2.88	8.18×10^{-4}	0.380	1.963
$Zn_{0.98}Mn_{0.01}Cu_{0.01}O$	0.062	−2.53	6.27×10^{-4}	0.379	1.965
$Zn_{0.97}Mn_{0.02}Cu_{0.01}O$	0.074	−1.48	8.31×10^{-4}	0.376	1.950
$Zn_{0.96}Mn_{0.03}Cu_{0.01}O$	0.063	−4.44	6.00×10^{-4}	0.379	1.957
$Zn_{0.95}Mn_{0.04}Cu_{0.01}O$	0.066	−3.40	7.28×10^{-4}	0.379	1.963
$Zn_{0.94}Mn_{0.05}Cu_{0.01}O$	0.068	−6.36	6.95×10^{-4}	0.379	1.948

second phase as delineated in the XRD spectra in Fig. 1.

Fig. 5 shows FT-IR transmittance spectra in the range 4000–400 cm^{-1} for all the powder samples. The absorption peaks observed between 2300 and 2400 cm^{-1} were due to the existence of CO_2 molecules in the air. The vibration bands discerned in the range of 420–550 cm^{-1} were ascribed to the vibration modes of Zn—Cu—Mn—O. Although the absorption bands were inherent in all powders, the absorption peak positions changed according to the doping concentration of Mn. The absorption band was observed in un-doped $Zn_{0.99}Cu_{0.01}O$ samples at 514 cm^{-1}. The absorption band of Zn—O stretching was shifted to 508 cm^{-1} when the Mn doping was increased from 1 to 5%. The increase in the manganese content resulted in the slight shift in the position of absorption band which might be due to the incorporation of the Mn and Cu dopant ions in the lattice structure of Zn—O [36]. The characteristic absorption band at 425 cm^{-1} was assigned to stretching modes of ZnO. Also, doping of larger ionic radii of $Mn2^+$ (0.66 Å) and Cu (0.73 Å) in place

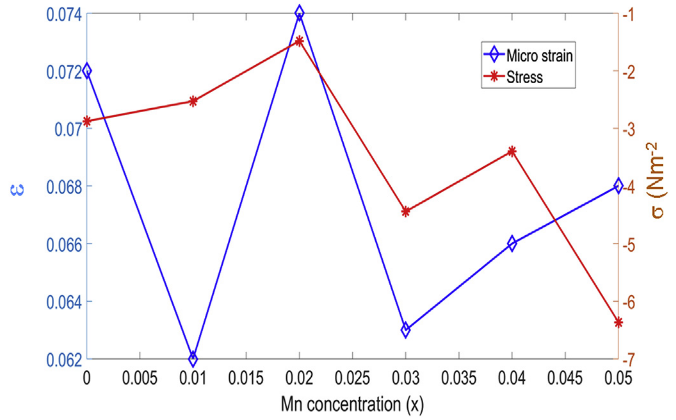

Fig. 4. Concentration-dependent micro strain (*ε*) and stress (σ) values in $Zn_{0.99\text{-}x}Mn_xCu_{0.01}O$ structures (x = 0.00, 0.01, 0.02, 0.03, 0.04, and 0.05).

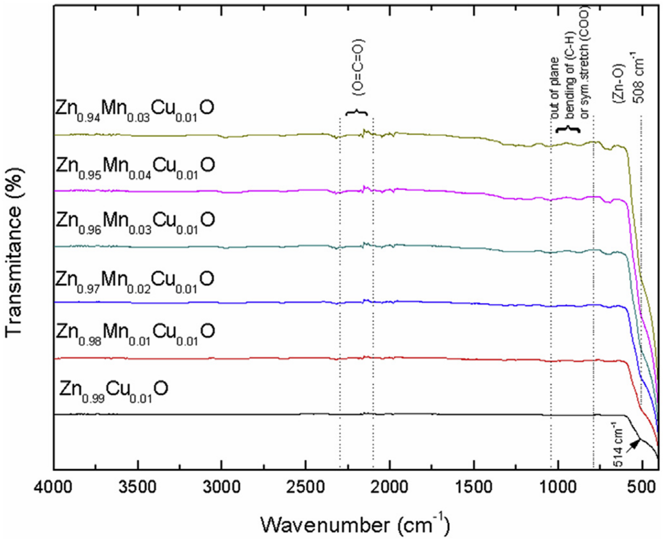

Fig. 5. FT-IR spectra of $Zn_{0.99-x}Mn_xCu_{0.01}O$ at different Mn concentrations.

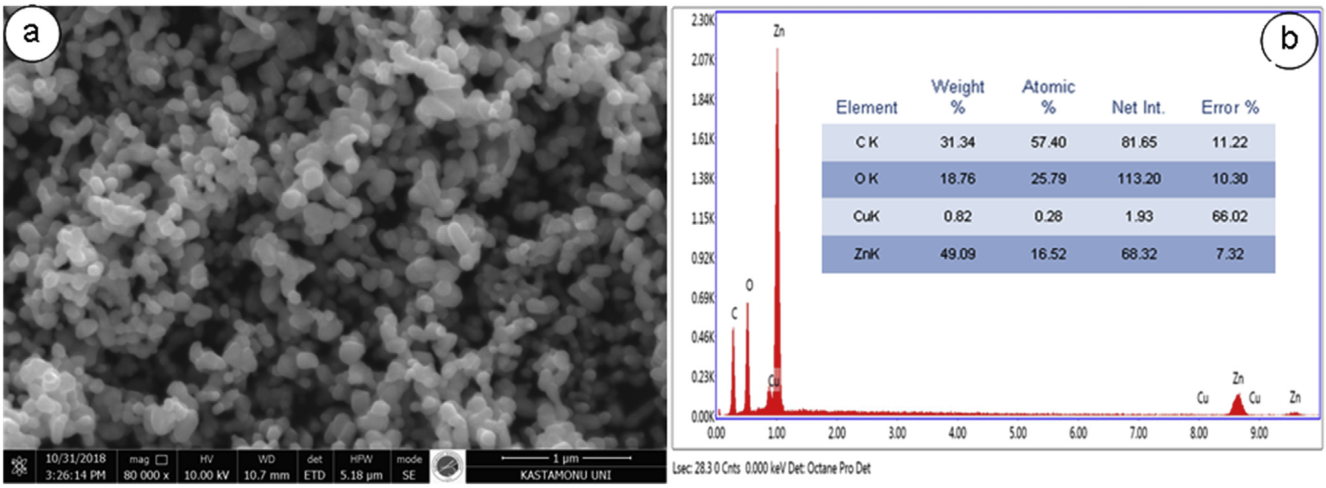

Element	Weight %	Atomic %	Net Int.	Error %
C K	31.34	57.40	81.65	11.22
O K	18.76	25.79	113.20	10.30
CuK	0.82	0.28	1.93	66.02
ZnK	49.09	16.52	68.32	7.32

Fig. 6. SEM image and EDAX spectra of $Zn_{0.99}Cu_{0.01}O$ nanoparticles.

of smaller ionic radii of Zn (0.60 Å) increased the bond length. Thus, these expanded bands absorbed the FT-IR frequencies at higher side than pure ZnO [36].

The surface particle distributions of ZnMnCuO nanoparticles sintered at 600 °C for 2 h are given in Figs. 6–11. The agglomeration increases and the crystallite sizes fluctuated as the Mn concentration was increased. These results were compatible with the calculations shown in Table 1. Cluster shape random agglomeration was observed in all frames of SEM images obtained at different magnifications as shown in Figs. 6–11. The compositions of the $Zn_{0.99-x}Mn_xCu_{0.01}O$ nanoparticles were analyzed by the EDAX spectrum. Zn, Cu, Mn, and O peaks were distinguishable in the EDAX spectrum. The contents of Zn, Cu, and Mn were compatible with the synthesized nanoparticles.

3.2. *Photoluminescence (PL)*

PL measurements of Mn/Cu co-doped ZnO nanoparticles were carried out when the nanoparticles were stimulated at 300 nm wavelength, and the emitted light was recorded at a wavelength range of 350 nm–800 nm. The results of the PL measurements may be found in Fig. 12. As can be seen from the PL graphs in Fig. 12, the luminescence values of all nanoparticles reach their maximum at around 368 nm. With larger wavelengths, various shoulder regions with peaks corresponding to different wavelengths emerge depending on the doping concentration of Mn.

The PL spectra of the nanoparticles were subjected to Gauss decomposition to determine the PL measurements. Gaussian decomposition was obtained by using “Fityk” software. The model of spectrum curves in Gaussian decomposition is given by $f(\lambda) = ae^{-(\lambda-b)^2/2c^2}$ and shown in Fig. 13.

As shown in Fig. 13, the sum of the nine main Gaussian decompositions of PL spectra was plotted versus emission wavelength for various concentrations of $Zn_{0.99-x}Mn_xCu_{0.01}O$ (x = 0.00, 0.01, 0.02, 0.03, 0.04, 0.05) nanoparticles. In addition, the emission wavelengths were increased from Peak 1 to Peak 9. The peak positions of these curves varied according to the concentration of $Zn_{0.99-x}Mn_xCu_{0.01}O$ nanoparticles as indicated in Table 3. The solid grey line labeled as “Model” represented the linear combination of nine Gaussian peaks. These peaks corresponded to different emissions which were two ultraviolet emissions (Peak 1 and Peak 2), two violet emissions (Peak 3 and Peak 4), a blue emission (Peak 5), a green emission (Peak 6) a yellow-orange (Peak 7), a red emission (Peak 8), and near-infrared (NIR) (Peak 9) as shown in Fig. 13; see also Table 3. As seen in Table 3, these peak locations changed

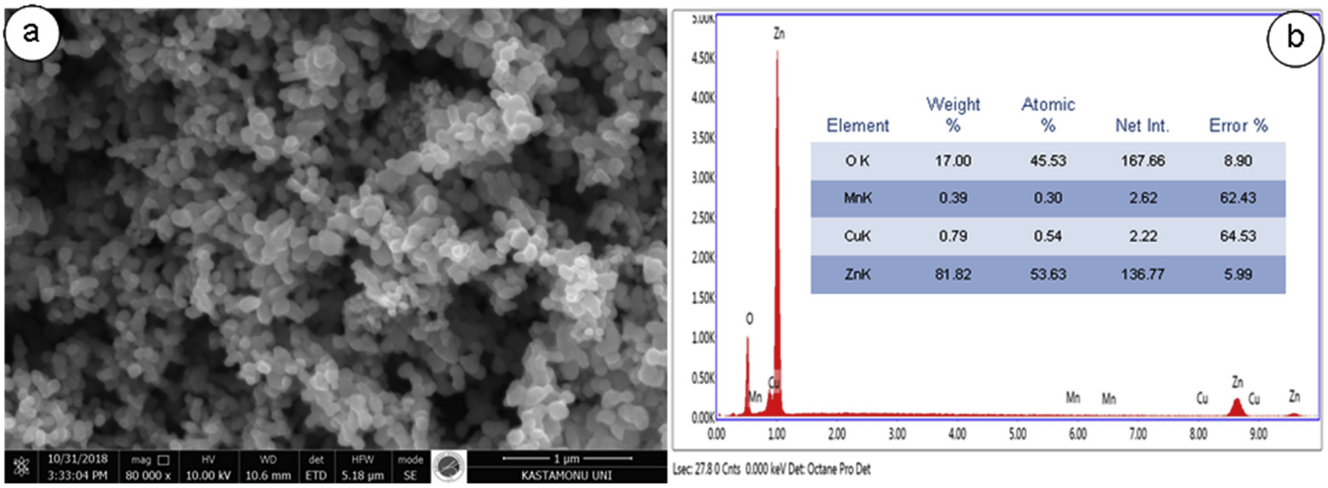

Element	Weight %	Atomic %	Net Int.	Error %
O K	17.00	45.53	167.66	8.90
MnK	0.39	0.30	2.62	62.43
CuK	0.79	0.54	2.22	64.53
ZnK	81.82	53.63	136.77	5.99

Fig. 7. SEM image and EDAX spectra of $Zn_{0.98}Mn_{0.01}Cu_{0.01}O$ nanoparticles.

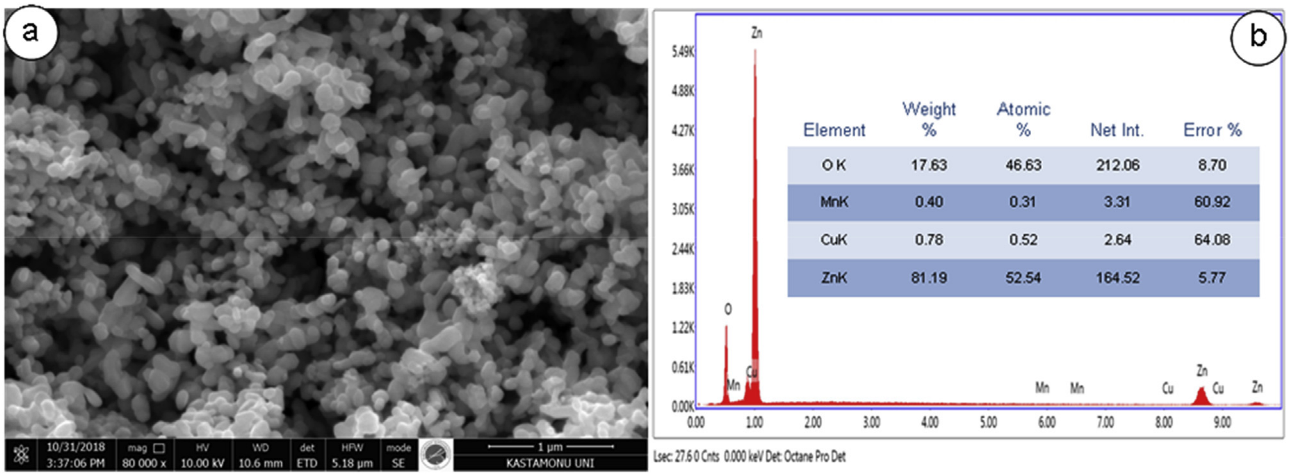

Element	Weight %	Atomic %	Net Int.	Error %
O K	17.63	46.63	212.06	8.70
MnK	0.40	0.31	3.31	60.92
CuK	0.78	0.52	2.64	64.08
ZnK	81.19	52.54	164.52	5.77

Fig. 8. SEM image and EDAX spectra of $Zn_{0.97}Mn_{0.02}Cu_{0.01}O$ nanoparticles.

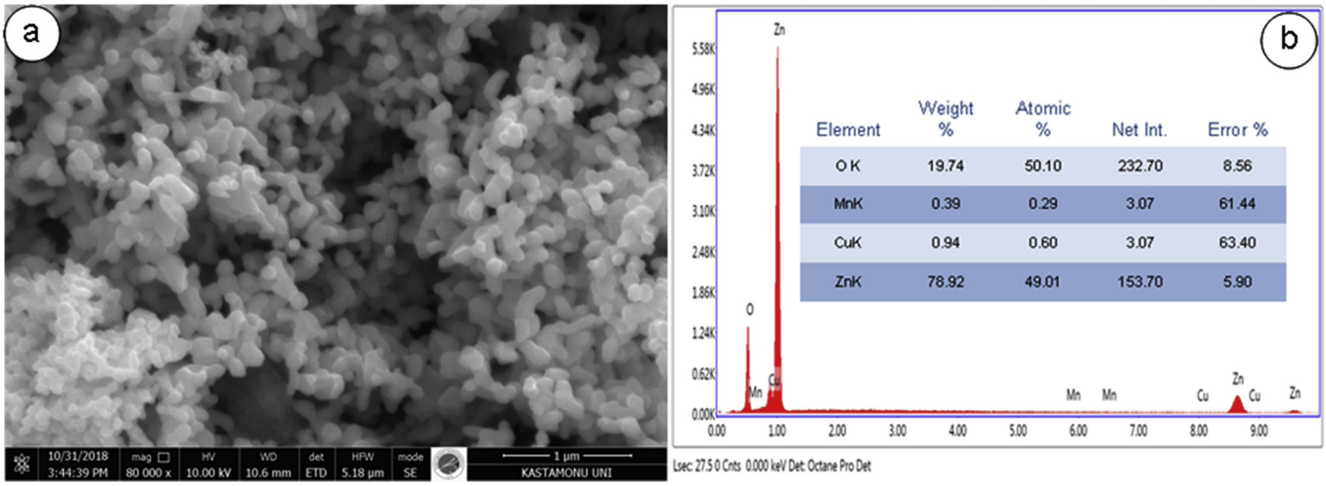

Element	Weight %	Atomic %	Net Int.	Error %
O K	19.74	50.10	232.70	8.56
MnK	0.39	0.29	3.07	61.44
CuK	0.94	0.60	3.07	63.40
ZnK	78.92	49.01	153.70	5.90

Fig. 9. SEM image and EDAX spectra of $Zn_{0.96}Mn_{0.03}Cu_{0.01}O$ nanoparticles.

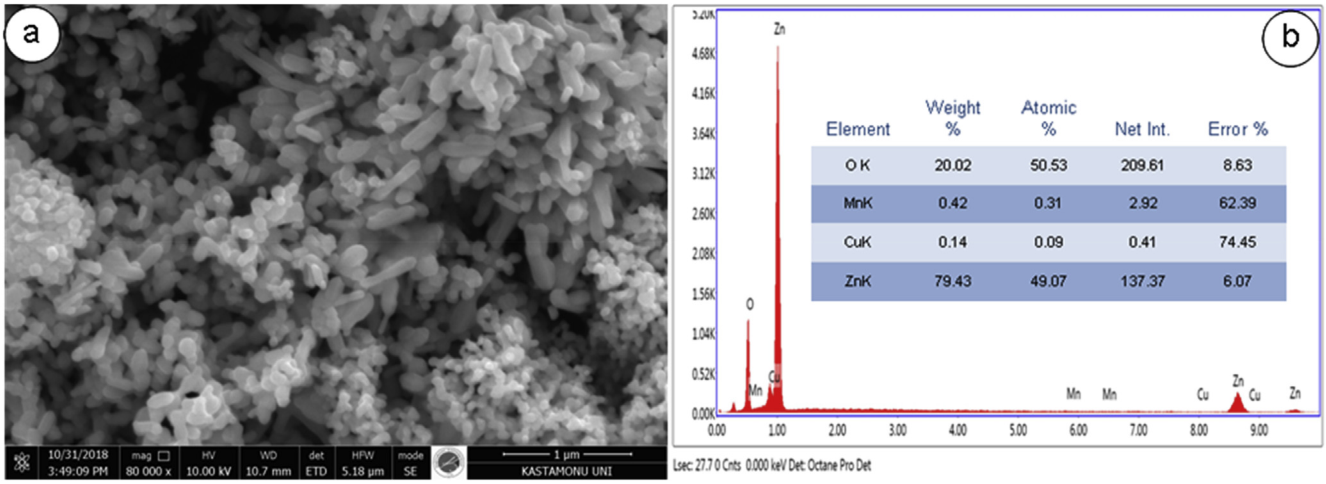

Element	Weight %	Atomic %	Net Int.	Error %
O K	20.02	50.53	209.61	8.63
MnK	0.42	0.31	2.92	62.39
CuK	0.14	0.09	0.41	74.45
ZnK	79.43	49.07	137.37	6.07

Fig. 10. SEM image and EDAX spectra of $Zn_{0.95}Mn_{0.04}Cu_{0.01}O$ nanoparticles.

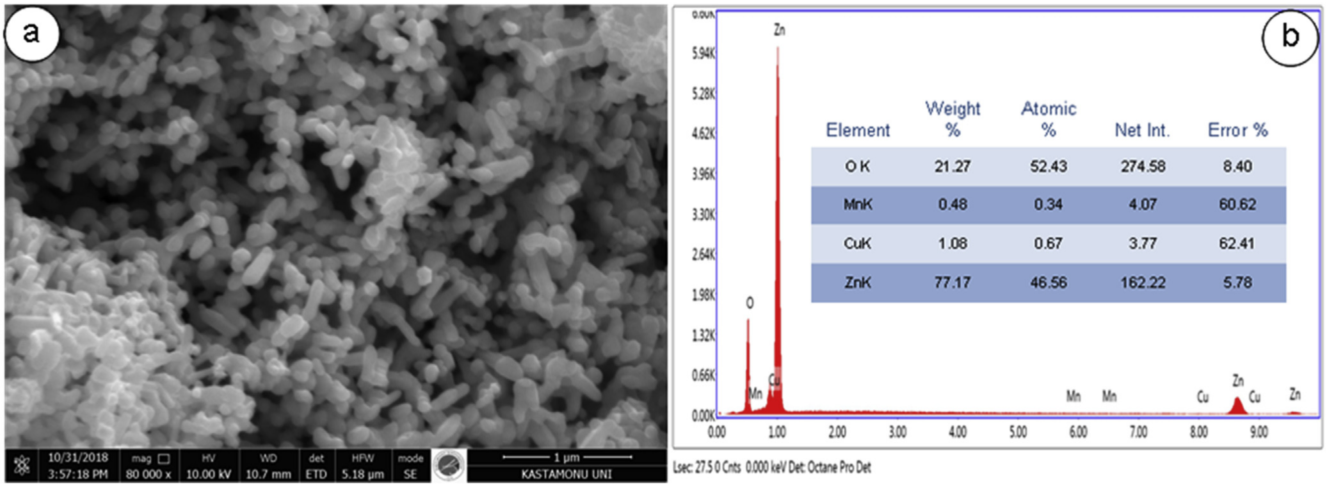

Element	Weight %	Atomic %	Net Int.	Error %
O K	21.27	52.43	274.58	8.40
MnK	0.48	0.34	4.07	60.62
CuK	1.08	0.67	3.77	62.41
ZnK	77.17	46.56	162.22	5.78

Fig. 11. SEM image and EDAX spectra of $Zn_{0.94}Mn_{0.05}Cu_{0.01}O$ nanoparticles.

depending on the concentration of Mn.

As shown in Figs. 12 and 13, the ultraviolet emission had the highest peaks compared to the other emissions. The global maximum height values appeared in the region of the ultraviolet (360–385 nm) for all samples, but there were also local maximums in the blue and green emissions (450–570 nm, for $x = 0.01$) and in the red emission (620–750 nm, for $x = 0.05$). Moreover, emission intensity values in the red emission were higher than the ones in the blue & green emissions as the concentration was increased. In other words, there was an inverse relation in the emission intensity values when we considered the blue & green emissions (450–570 nm) and the red emission (620–750 nm).

In Table 3, the emission regions could be interpreted as the following: Ultraviolet emissions (360–385 nm) might be attributed to the NBE of ZnO as an indication of the excitonic characteristic; violet-blue emissions (386–492 nm) might be ascribed to the transition of electrons from zinc interstitials to the valence band; green-yellow-orange emissions (520–560 nm; 560–610 nm) could be due to the single charged oxygen vacancy (V_o^{+}) and double charged oxygen vacancy (V_o^{++}), respectively. The findings of Xu et al. [37] may shed light in the case of the red emission (620–750 nm). Their findings demonstrated that the red emission from 620 to 690 nm could be attributed to oxygen interstitials (O_i) and the one in the range of 690–750 nm to oxygen vacancy (V_o).

Finally, the NIR region (750–768 nm) was related to the secondary UV diffraction [38–43]. Evidence of the NIR Peak 9 (750 nm) was observed by Lv et al. [39], Cross et al. [40], and Zhu et al. [41] and it might be caused by an oxygen vacancy. This NIR peak could also be ascribed to the second-order diffraction (a harmonic of the Peak 1 at 365 nm) of a near band-edge as stated in Shinagawa et al. [43].

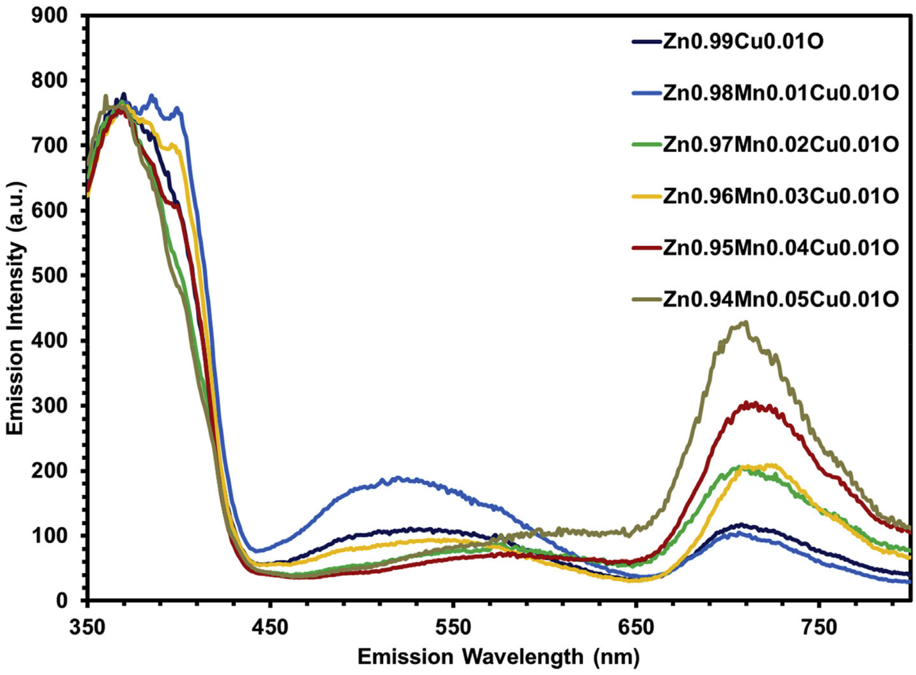

Fig. 12. PL spectra depending on the concentration of $Zn_{0.99-x}Mn_xCu_{0.01}O$ ($x = 0.00, 0.01, 0.02, 0.03, 0.04, 0.05$) nanoparticles prepared by solid state reaction method.

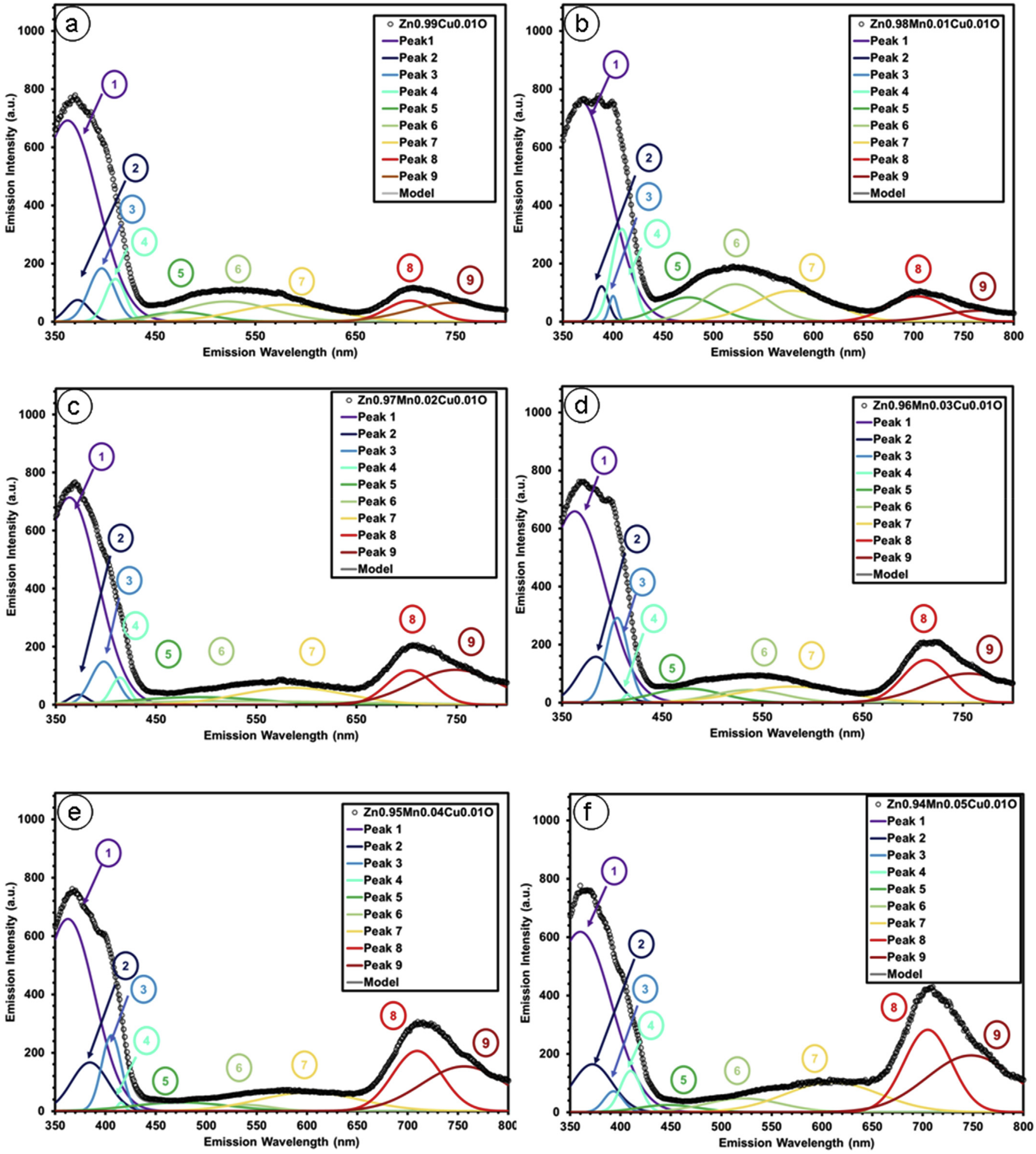

Fig. 13. Gaussian decompositions of PL spectra of the concentration of $Zn_{0.99-x}Mn_xCu_{0.01}O$ a) x = 0.00, b) x = 0.01, c) x = 0.02, d) x = 0.03, e) x = 0.04, and f) x = 0.05 nanoparticles.

3.3. *Optical studies*

3.3.1. *UV–VIS diffuse reflectance spectra*

The reflectance spectra of the $Zn_{0.99-x}Mn_xCu_{0.01}O$ (x = 0.00, 0.01, 0.02, 0.03, 0.04, 0.05) nanoparticles, obtained by UV–VIS diffuse reflectance measurements (DRS) within the range of 300–700 nm wavelength, are shown in Fig. 14. Notice that all the graphs in Fig. 14 have an absorption edge close to 365 nm, a wavelength similar to the band gap of ZnO. Maximum reflectance was observed for $Zn_{0.96}Mn_{0.03}Cu_{0.01}O$ nanoparticles.

3.3.2. *Band gap calculation*

The optical band gap E_g can be determined using the following equation for the absorption coefficient (α) and the photon energy ($h\nu$):

Table 3
Comparison of centers of PL emission values (a.u.) of $Zn_{0.99-x}Mn_xCu_{0.01}O$ (x = 0.00, 0.01, 0.02, 0.03, 0.04, 0.05) nanoparticles.

Peak Label	x = 0.0	x = 0.01	x = 0.02	x = 0.03	x = 0.04	x = 0.05	Emission range
Peak 1	362.6	368	363.3	362.6	362.6	360	Ultraviolet
Peak 2	372.6	388.5	372.4	383.5	384.4	372	Ultraviolet
Peak 3	396.7	399.9	397.6	404.9	405.8	393	Violet
Peak 4	410.3	408.7	413.8	415.5	415.5	410	Violet
Peak 5	475	475.2	491.7	475	475	447	Blue
Peak 6	522	521.9	525.6	536.4	537.3	522	Green
Peak 7	580	579.3	586.5	579.4	602.3	610	Yellow-Orange
Peak 8	704.4	703.1	703.6	713.3	709.4	705	Red
Peak 9	748.3	767.5	748.6	755.9	756	748	NIR (near-infrared)

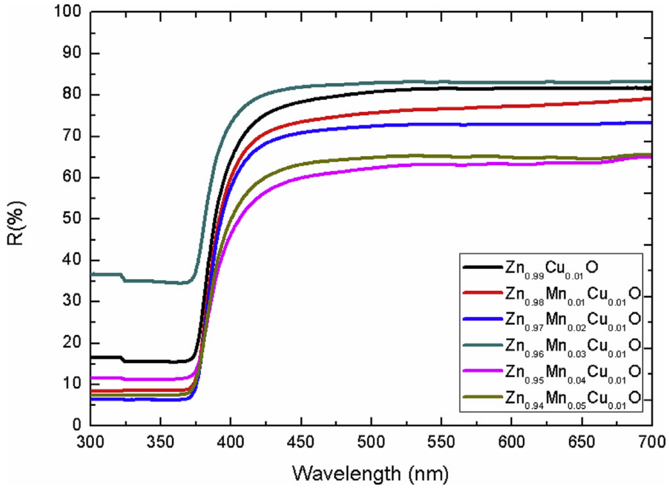

Fig. 14. The reflectance spectra of the $Zn_{0.99-x}Mn_xCu_{0.01}O$ nanoparticles at different Mn concentrations.

Table 4
Fitting the curve function $y(h\upsilon) = A \times h\upsilon + B$, band gap energies E_g (eV) and relative errors for different Mn doping ratios for the $Zn_{0.99\text{-}x}Mn_xCu_{0.01}O$ (x = 0.00, 0.01, 0.02, 0.03, 0.04, 0.05) nanoparticles.

Sample Name	A	B	E_g (eV)	Rel. Error
$Zn_{0.99}Cu_{0.01}O$	750.3	−2444.8	3.26	1.2×10^{-2}
$Zn_{0.98}Mn_{0.01}Cu_{0.01}O$	3178.06	−10387.73	3.27	1.8×10^{-2}
$Zn_{0.97}Mn_{0.02}Cu_{0.01}O$	6567.78	−21523.66	3.28	1.6×10^{-2}
$Zn_{0.96}Mn_{0.03}Cu_{0.01}O$	49.29	−160.09	3.25	1.5×10^{-2}
$Zn_{0.95}Mn_{0.04}Cu_{0.01}O$	1370.01	−4446.37	3.25	1.9×10^{-2}
$Zn_{0.94}Mn_{0.05}Cu_{0.01}O$	3872.65	−12661.91	3.27	1.6×10^{-2}

$$\alpha h\upsilon = \mathrm{k}(\mathrm{h}\upsilon - E_g)^{1/n} \tag{5}$$

In Eq. (5), E_g and k are the optical band gap and energy-independent constants, respectively. Since $F(R_\alpha)$ is proportional to α and ZnO has directly allowed transitions, n is taken as 1/2. Thus, Eq. (5) can be transformed to:

$$F(R_\alpha)\, h\upsilon = \mathrm{k}(\mathrm{h}\upsilon - E_g)^{1/2} \tag{6}$$

in other words, $(F(R_\alpha)\, h\upsilon)^2 = k^2(\mathrm{h}\upsilon - E_g)$. The slope of the graph of $(F(R_\alpha)\, h\upsilon)^2$ was approximated by using a linear fit $y(h\upsilon) = A \times h\upsilon + B$ in the least-squares sense between 350 and 400 nm. To do this, the following error formula given in Eq. (7)

$$E(A,B) = \min_{A,\,B} \sum_{i=1}^{N} \left[A \times (h\upsilon)_i + B - \left((F(R_\alpha)\, h\upsilon)^2\right)_i\right]^2 \tag{7}$$

was minimized for A and B where N is the number of data points. Table 4 displays A, B, band gap energies E_g and relative error values for these data set.

The band gap energies E_g, as shown in Table 4 and Fig. 15 a - f, were calculated by the linear approximation of the slope of the graph of $(F(R_\alpha)\, h\upsilon)^2$ to the photon energy axis where $F(R_\alpha) = 0$, namely, $E_g = h\upsilon = -\frac{B}{A}$, as plotted in Fig. 15 a - f. In other words, the intersection between the linear fit and the photon energy axis gave the value to E_g. From Fig. 15 a - f, the band gap energies of the Mn-doped $ZnCu_{0.01}O$ nanoparticles samples were observed in the range of 3.25 and 3.28 eV which were accurate within two decimal digits. These changes in the values of E_g depended on several factors such as crystallite size, carrier concentration, lattice strain, and the size effect of the dopant metals in ZnO lattice [38].

As seen in Tables 1 and 4, there was an inverse relation between the energy band gap and cell volume. The maximum band gap appeared at 2% Mn concentration with value of 3.28 eV and the maximum cell volume was found at 1% Mn concentration with a value of 46.35 Å^{3}.

3.3.3. *Refractive index calculation*

High refractive index n and wide band gap E_g are the main goals of the recent studies due to their applications in optoelectronic and sensor industries.

Fig. 15 a - f exhibit the variations in the refractive indices of these five models obtained by altering the Mn concentration and Table 5 presents the pertinent calculated values. According to the findings of Naccarato et al. [1] (See Fig. 5 therein), our material ($n > 2$ and $E_g > 3$) considered in this research was classified as Transition Metals (TMs) with an empty d shell (e.g. V^{5+}).

We calculated the refraction index based on the following five models:

Ravindra et al. [2] $n = 4.084 - 0.62\, E_g$, Moss [3] $n = \left(\frac{95}{E_g}\right)^{\frac{1}{4}}$,

Hervé and Vandamme [4] $n = \sqrt{1 + \left(\frac{13.6}{E_g + 3.47}\right)^2}$,

Reddy and Anjayenulu [5] $n = \left(\frac{154}{E_g - 0.365}\right)^{\frac{1}{4}}$, and finally.

Kumar and Singh [6] $n = 3.3668\, (E_g)^{-0.32234}$ and listed the calculated data in Table 5. It can be noted in the above models except that of Ravindra that the refractive index is inversely proportional to the band gap energy; in other words, $n \approx \left(\frac{1}{E_g}\right)^k$, $0.25 < k < 1$.

Fig. 16 shows that all five models possess the same pattern between the energy band gap and refractive index. Among these five models, Moss [3] and Kumar and Singh [6] gave similar results in the range of 2.30–2.33. In 2015, Tripathy gave the following

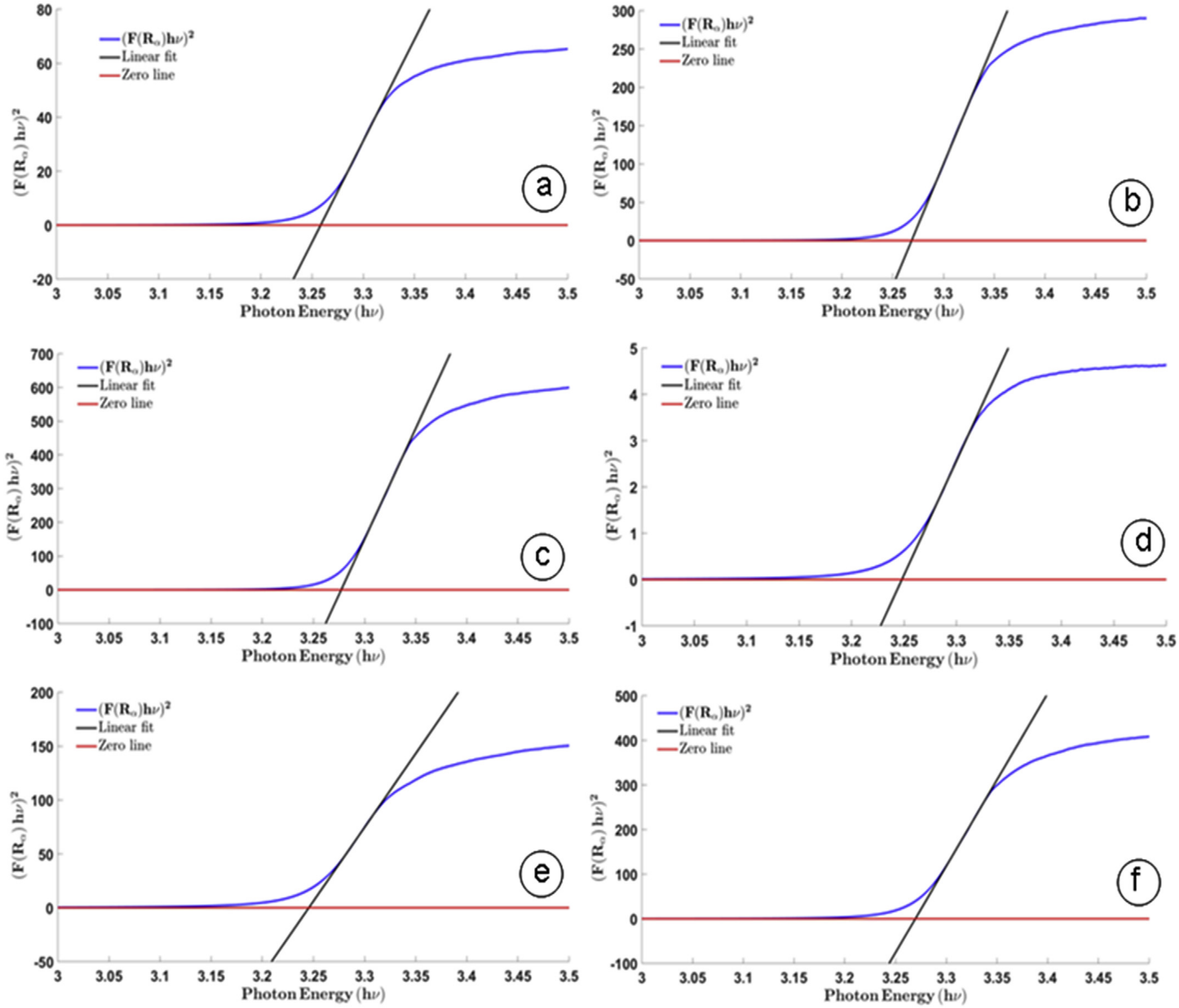

Fig. 15. The plots of $(F(R_\alpha)h\nu)^2$ as a function of photon energy (hν) and the linear fit for the a) $Zn_{0.99-x}Mn_xCu_{0.01}O$ for x = 0.00 b) $Zn_{0.99-x}Mn_xCu_{0.01}O$ for x = 0.01 c) $Zn_{0.99-x}Mn_xCu_{0.01}O$ for x = 0.02 d) $Zn_{0.99-x}Mn_xCu_{0.01}O$ for x = 0.03 e) $Zn_{0.99-x}Mn_xCu_{0.01}O$ for x = 0.04 f) $Zn_{0.99-x}Mn_xCu_{0.01}O$ for x = 0.05 nanoparticles.

reliability ranges for the energy band gaps based on these five models [44] and these values were listed in Table 6.

As shown in Table 5, our calculated energy band gap values were in the range of 3.25 eV and 3.28 eV, thus refractive index values based on these models were valid. Moreover, in 2016, Chithra and Pushpanathan studied optical properties of Cu-doped ZnO particles and found the energy band gap as 3.31 eV and refractive index as 1.9958 for 1% Cu concentration [41]. Table 5 showed that the method of Ravindra et al. [2] gave similar results to those of Chithra and Pushpanathan [45].

4. Conclusions

$Zn_{0.99-x}Mn_xCu_{0.01}O$ (x = 0.00, 0.01, 0.02, 0.03, 0.04, and 0.05) nanoparticles were prepared by the solid state reaction method. Its structural, microstructural, and optoelectronic properties were

Table 5
Refractive indices calculated by different methods using band gap energies with Mn concentration accurate within two decimal digits.

Sample Name	Ravindra et al.	Moss	Hervé and Vandamme	Reddy and Anjayenulu	Kumar and Singh
$Zn_{0.99}Cu_{0.01}O$	2.06	2.32	2.26	2.70	2.30
$Zn_{0.98}Mn_{0.01}Cu_{0.01}O$	2.06	2.32	2.25	2.70	2.30
$Zn_{0.97}Mn_{0.02}Cu_{0.01}O$	2.05	2.32	2.25	2.70	2.30
$Zn_{0.96}Mn_{0.03}Cu_{0.01}O$	2.07	2.33	2.26	2.70	2.30
$Zn_{0.95}Mn_{0.04}Cu_{0.01}O$	2.07	2.33	2.26	2.70	2.30
$Zn_{0.94}Mn_{0.05}Cu_{0.01}O$	2.06	2.32	2.25	2.70	2.30

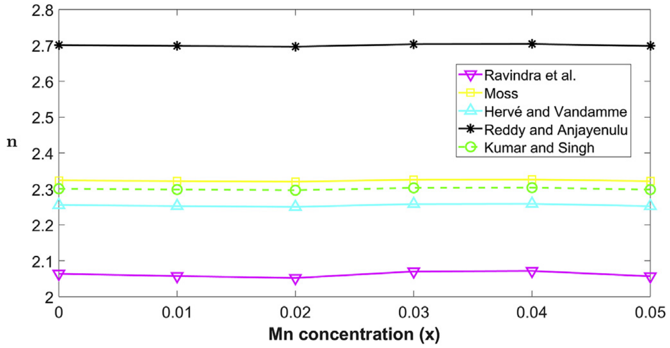

Fig. 16. Refractive index as a function of Mn concentration (x) of $Zn_{0.99\text{-}x}Mn_xCu_{0.01}O$ structures using all five different models.

Table 6
Reliability ranges for the energy band gaps based on the models.

Model	Reliability Ranges of Band Gaps
Ravindra et al.	1.50 eV < E_g < 3.50 eV
Moss	0.17 eV < E_g < 3.68 eV
Hervé and Vandamme	2.00 eV < E_g < 4.00 eV
Reddy and Anjayenulu	1.10 eV < E_g < 6.20 eV
Kumar and Singh	2.00 eV < E_g < 4.00 eV

analyzed according their concentration levels. X-ray diffraction analysis showed the ZnO phase with wurtzite hexagonal structure as the first phase and Mn_2O_3 as the second. Moreover, the fluctuations in the strain and stress values might be used to reveal many physical defects and dislocations in the host lattice structure. At $x = 0.03$, the maximum crystallite size (40.82 nm) occurred and dislocation density (δ) had the minimum value of 6.0×10^{-4}. The PL measurements showed the red emission with its wavelength within the range of 620–750 nm. This range can be classified into two parts; the red emission from 620 to 690 nm can be attributed to oxygen interstitials (O_i) and this phenomenon is commonly observed. However, the red emission in the range of 690–750 nm may be due to oxygen vacancy (V_o) which strongly is dependent on the Mn concentration and this event is rarely observed.

For 2% Mn concentration, the maximum band gap occurred with a band gap energy of $E_g = 3.28$ eV and the crystallite size was minimum (34.70 nm) since the value of c/a was the closest value to the ideal value of 1.63 at $x = 0.02$. The refractive index values were in the range of 2.05 and 2.7. This property might make Mn/Cu co-doped ZnO nanoparticles strong candidates for device applications.

CRediT author statement

S. D. Senol: Sample Preparation, XRD, FTIR, and UV–VIS diffuse reflectance measurements. E. Ozugurlu: Curve fitting and Writing Draft Preparation, Writing-Reviewing and Editing, L. Arda: Conceptualization, Methodology, Writing- Original draft preparation, Validation, Writing- Reviewing and Editing, XRD, SEM, EDS, PL and optical properties measurements and discussions.

Declaration of competing interests

The authors declare that they have no known competing financial interests or personal relationships that could have appeared to influence the work reported in this paper.

Acknowledgements

This research was supported by the Bolu Abant İzzet Baysal University Scientific Research Projects under Project No: BAP-2018.03.03.1320, Bolu, Turkey and the Research Fund of Bahcesehir University under the Project No: BAU-BAP.2018.02.16, Istanbul, Turkey.

References

[1] F. Naccarato, F. Ricci, J. Suntivich, G. Hautier, L. Wirtz, G.-M. Rignanese, Searching for materials with high refractive index and wide band gap: a first-principles high-throughput study, Phys. Rev. Mater. 3 (2019), 044602.

[2] N.M. Ravindra, S. Auluck, S, V.K. Srivastava, On the penn gap in semiconductors, Phys. Status Solidi B 93 (2) (1979) K155–K160.

[3] T.S. Moss, Relations between the refractive index and energy gap of semiconductors, Phys. Status Solidi B 131 (1985) 415.

[4] P. Hervé, L. Vandamme, General relation between refractive index and energy gap in semiconductors, Infrared Phys. Technol. 35 (1994) 609.

[5] R.R. Reddy, S. Anjaneyulu, Analysis of the Moss and Ravindra relations, Phys. Status Solidi B 174 (1992) K91.

[6] V. Kumar, J. Singh, Model for calculating the refractive index of different materials, Indian J. Pure Appl. Phys. 48 (2010) 571.

[7] S. Noda, M. Fujita, T. Asano, Spontaneous-emission control by photonic crystals and nanocavities, Nat. Photonics 1 (2007) 449–458.

[8] S.P. Hoffmann, M. Albert, N. Weber, D. Sievers, J. Förstner, T. Zentgraf, C. Meier, Tailored UV emission by nonlinear IR excitation from ZnO photonic crystal nanocavities, ACS Photonics 5 (5) (2018) 1933–1942.

[9] L. Chen, X. Zhang, Z. Xiong, Y. Liu, Y. Cui, B. Liu, Noble metal dopants modified two-dimensional zinc oxide: electronic structures and magnetic properties, J. Alloy. Comp. 798 (2019) 149–157.

[10] R. Yoo, Y. Park, H. Jung, H.J. Rim, S. Cho, H.S. Lee, W. Lee, Acetone-sensing properties of doped ZnO nanoparticles for breath-analyzer applications, J. Alloy. Comp. 803 (2019) 135–144.

[11] Y. Kim, M. Chang, S. Cho, M. Kim, H. Kim, E. Choi, H. Ko, J. Hwang, B. Park, Formation of a functional homo-junction interface through ZnO atomic layer passivation: enhancement of carrier mobility and threshold voltage in a ZnO nanocrystal field effect transistor, J. Alloy. Comp. 804 (2019) 213–219.

[12] J.S. Jang, J. Kim, U. Ghorpade, H.H. Shin, M.G. Gang, S.D. Park, H. Kim, D.S. Lee, J.H. Kim, Comparison study of ZnO-based quaternary TCO materials for photovoltaic application, J. Alloy. Comp. 793 (2019) 499–504.

[13] S.Y. Yurish, Advances in Microelectronics: Reviews, ume 1, IFSA Publishing, Barcelona, 2018.

[14] Z. Huang, Y. Yan, C. Xing, Q. Wang, J. Li, Y. Zhang, Y. Zeng, Y. Zhao, Y. Jiang, Enhanced properties of hierarchically-nanostructured undoped acceptor-rich ZnO single-crystal microtube irradiated by UV laser, J. Alloy. Comp. 789 (2019) 841–851.

[15] P. Meng, X. Zhao, Z. Fu, J. Wu, J. Hu, J. He, Novel zinc-oxide varistor with superior performance in voltage gradient and aging stability for surge arrester, J. Alloy. Comp. 789 (2019) 948–952.

[16] M.F.M. Noh, N.A. Arzaee, J. Safaei, N.A. Mohamed, H.P. Kim, A.R.M. Yusoff, J. Jang, M.A.M. Teridi, Eliminating oxygen vacancies in SnO2 films via aerosol-assisted chemical vapor deposition for perovskite solar cells and photoelectrochemical cells, J. Alloy. Comp. 773 (2019) 997–1008.

[17] E. Asikuzun, O. Ozturk, L. Arda, C. Terzioglu, Preparation, growth and characterization of nonvacuum Cu-doped ZnO thin films, J. Mol. Struct. 1165 (2018) 1–7.

[18] A. Guler, L. Arda, N. Dogan, C. Boyraz, E. Ozugurlu, The annealing effect on microstructure and ESR properties of (Cu/Ni) co-doped ZnO nanoparticles, Ceram. Int. 45 (2) (2019) 1737–1745.

[19] C. Boyraz, N. Dogan, L. Arda, Microstructure and magnetic behavior of (Mg/Ni) co-doped ZnO nanoparticles, Ceram. Int. 43 (17) (2017) 15986–15991.

[20] M. Tosun, L. Arda, Effect of temperature and film thickness on structural and mechanical properties of c-axis oriented $Zn_{0.95}Mg_{0.05}O$ thin films, Ceram. Int. 45 (13) (2019) 16234–16243.

[21] I.P. Duru, E. Ozugurlu, L. Arda, Size effect on magnetic properties of $Zn_{0.95-x}Mg_xNi_{0.05}O$ nanoparticles by Monte Carlo simulation, Ceram. Int. 45 (2019) 5259–5265.

[22] S.D. Senol, C. Boyraz, E. Ozugurlu, A. Gungor, L. Arda, Band gap engineering of Mg doped ZnO nanorods prepared by a hydrothermal method, Cryst. Res. Technol. 54 (3) (2019) 1800233.

[23] D. Ficai, A.M. Grumezescu (Eds.), Nanostructures for Novel Therapy: Synthesis, Characterization and Applications, Elsevier, 2017.

[24] A.J. Reddy, M.K. Kokila, H. Nagabhushan, R.P.S. Chakradhar, C. Shivakumar, J.L. Rao, B.M. Nagabhushan, Structural, optical and EPR studies on ZnO: Cu nanopowders prepared via low temperature solution combustion synthesis, J. Alloy. Comp. 509 (2011) 5349–5355.

[25] Y.M. Tao, S.Y. Ma, H.X. Chen, J.X. Meng, L.L. Hou, Y.F. Jia, X.R. Shang, Effect of the oxygen partial pressure on the microstructure and optical properties of ZnO: Cu films, Vacuum 85 (2011) 744–748.

[26] S. Kumar, S. Chatterjee, K.K. Chattopadhyay, A.K. Ghosh, Sol–Gel-Derived ZnO:Mn nanocrystals: study of structural, Raman, and optical properties, J. Phys. Chem. C 116 (2012) 16700.

[27] N. Tiwari, S. Kumar, C. Kamal, A. Chakrabarti, C. Lal Prajapat, P.K. Mishra, P. Mondal, S. Nath Jha, D. Bhattacharyya, Structural investigations of (Ni, Cu) Co–doped ZnO nanocrystals by X-ray absorption spectroscopy, Chem. Sel. 3 (20) (2018) 5644–5651.

[28] D. Sharma, R. Jha, Transition metal (Co, Mn) co-doped ZnO nanoparticles: effect on structural and optical properties, J. Alloy. Comp. 698 (2017) 532–538.

[29] D.K. Dubey, D.N. Singh, S. Kumar, C. Nayak, P. Kumbhakar, S.N. Jha, D. Bhattacharya, A.K. Ghosh, S. Chatterjee, Local structure and photocatalytic properties of sol-gel derived Mn-Li co-doped ZnO diluted magnetic semiconductor nanocrystals, RSC Adv. 6 (2016) 22852–22867.

[30] T. Tamura, H. Ozaki, The relationship of the magnetic properties of M (M = Mn, Fe, Co)-doped ZnO single crystals and their electronic structures, J. Condens. Matter. Phys. 21 (2) (2009), 026009.

[31] H.T. Cao, Z.L. Pei, J. Gong, C. Sun, R.F. Huang, L.S. Wen, Preparation and characterization of Al and Mn doped ZnO (ZnO:(Al, Mn)) transparent conducting oxide films, J. Solid State Chem. 177 (2004) 1480.

[32] V.D. Mote, Y. Purushotham, B.N. Dole, Structural, morphological, physical and dielectric properties of Mn doped ZnO nanocrystals synthesized by sol–gel method, Mater. Des. 96 (2016) 99–105.

[33] R.D. Shannon, C.T. Prewitt, Effective ionic radii and crystal chemistry, J. Inorg. Nucl. Chem. 32 (1970) 1427.

[34] A.K. Srivastava, J. Kumar, Effect of zinc addition and vacuum annealing time on the properties of spin-coated low-cost transparent conducting 1 at % Ga–ZnO thin films, Sci. Technol. Adv. Mater. 14 (2013), 065002.

[35] B.D. Cullity, S.R. Stock, Elements of X-Ray Diffraction, third ed., Prentice Hall, New Jersey, 2001.

[36] M. Ashokkumar, S. Muthukumaran, Structural, morphological and spectroscopic investigation of Mn doped $Zn_{0.96}Cu_{0.04}O$ nanoparticles, J. Mater. Sci. 26 (2015) 1225–1233.

[37] L. Xu, G. Zheng, J. Wang, F. Xian, Y. Liu, Stable co-emission of UV, green and red light in ZnO thin films with rapid annealing treatment, Opt. Int. J. Light Electron Opt. 127 (2016) 5942–5949.

[38] S. Muthukumaran, R. Gopalakrishnan, Structural, FT-IR and photoluminescence studies of Cu doped ZnO nanopowders by co-precipitation method, Opt. Mater. 34 (2012) 1946–1953.

[39] J.G. Lv, C.L. Liu, W.B. Gong, Z.F. Zi, X.S. Chen, K. Huang, T. Wang, G. He, S.W. Shi, X.P. Song, Z.Q. Sun, Temperature-dependent shifts of near band-edge emission and their second-order diffraction for ZnO nanorods, Opt. Mater. 34 (2012) 1917–1920.

[40] R.B.M. Cross, M.M. De Souza, E.M.S. Narayanan, A low temperature combination method for the production of ZnO nanowires, J. Nanotechnol. 16 (2005) 2188.

[41] Y. Zhu, C.H. Sow, T. Yu, Q. Zhao, P. Li, Z. Shen, D. Yu, J.T.L. Thong, Co-synthesis of ZnO–CuO nanostructures by directly heating brass in air, Adv. Funct. Mater. 16 (2006) 2415.

[42] G.H. Mhlongo, K. Shingange, Z.P. Tshabalala, B.P. Dhonge, F.A. Mahmoud, B.W. Mwakikunga, D.E. Motaung, Room temperature ferromagnetism and gas sensing in ZnO nanostructures: influence of intrinsic defects and Mn Co, Cu doping, Appl. Surf. Sci. 390 (2016) 804–815.

[43] T. Shinagawa, S. Watase, M. Izaki, Size-controllable growth of vertical ZnO nanorod arrays by a Pd-catalyzed chemical solution process, Cryst. Growth Des. 11 (2011) 5533.

[44] S. Tripathy, Refractive indices of semiconductors from energy gaps, Opt. Mater. 46 (2015) 240–246.

[45] M.J. Chithra, K. Pushpanathan, Thermal, structural and optical investigation of Cu-doped ZnO nanoparticles, Mod. Phys. Lett. B 30 (2016) 1650406. B 30 (34.